

4. Barringer Meteorite Impact Crater



Barringer Meteorite Crater has a diameter of ~1.2 km (Fig. 4.1 and 4.2). It is topographically defined by a rim that rises 30 to 60 m above the surrounding plain and a bowl-shaped depression that is ~180 m deep. The upper crater walls have average slopes of ~40 to ~50°, although they also include vertical to near-vertical cliffs (Fig. 4.2 and 4.3). The crater floor is below the surrounding plain, which is a feature that distinguishes Barringer Crater from most volcanic structures where craters are perched on volcanic summits (*e.g.*, cinder cones, shield volcanoes, and stratovolcanoes). Volcanic maars are the principal exception.

The crater has a simple bowl-shaped morphology, which is the classic “simple” crater morphology that characterizes impact craters that are $\lesssim 2$ km diameter in sedimentary targets and $\lesssim 4$ km diameter in crystalline targets (under Earth’s gravity). In contrast, larger “complex” craters may have central peaks, central peak rings, modification zones where the crater walls extensively collapse, and possibly external structural deformational rings.

Tear faults cross-cut the crater in four areas, producing “corners” that give the crater a squared shape in plan view, rather than a circular one. The region was cross-cut by a strong set of SE-NW joints and a weaker set of SW-NE joints prior to impact (Shoemaker, 1960; Roddy, 1978), which are generally thought to have been activated into tear faults during the excavation phase of the crater forming event.

Shoemaker (1960) produced the definitive geologic map of the crater (Fig. 4.4), which illustrates the target lithologies in the crater walls and the redistribution of target lithologies in a surrounding ejecta blanket. It also shows that the upper crater walls and uplifted crater rim are composed of Coconino, Toroweap, Kaibab, Moenkopi, and debris from those units. Debris also occurs within the crater in the form of complex breccia deposits that Shoemaker (1960) mapped as three units: authigenic breccia, allogenic breccia, and mixed debris.

Authigenic breccias are monomict, intraformational breccias that are caused by disruptive shear within formations (*e.g.*, Kaibab). This type of breccia is present along faults that cross-cut the crater walls and crater rim.

Allogenic breccias are sometimes dominated by components from a single formation, but in other cases are composed of fragments from multiple formations. These breccia deposits are displaced, however, having flowed down crater walls. They also contain shock-melted Coconino (lechatelierite) and meteoritic debris. Remnants of these breccias occur on upper crater walls, but they also flowed downward to form a thick breccia lens at the bottom of the crater (Fig. 4.5). Shoemaker (1974) suggested that downward flows of allogenic breccia converged on the crater floor to form a “central peak” beneath Silica Hill. Where exposed in crater walls, the allogenic breccia is dominated by debris from the Kaibab Formation. In the breccia lens on the crater floor, however, the breccia is dominated by fragments from the Coconino Formation. As illustrated in the W-E cross-section of Fig 4.5, the lens of allogenic breccia on the crater floor is generally believed to conform to a hemispherical transient crater. As discussed below, however, the subsurface extent of the breccia is still uncertain.

Stratigraphically above and resting on the allogenic breccia is a unit Shoemaker (1960) called “mixed debris.” This unit contains material from all four formations, including all five stages of shocked Coconino sandstone (as defined by Kieffer, 1971), plus meteoritic debris. In one of the deposits that outcrops along the east crater wall, Shoemaker (1974) also described lapilli of shock-melted Kaibab

dolomite. Although not described by Shoemaker, I have also found fragments of vesicular mixed melts in that breccia. Shoemaker interpreted this mixed debris unit to be fall-out material. That is, material blasted into the atmosphere above the crater and then re-deposited on top of the crater after it was excavated. Shoemaker (1960) only found this material within the crater. Exposed patches are found along the upper crater walls and a 10.5 m (35 ft) thick layer sits on top of the allogenic breccia on the crater floor. This latter unit appears to be normally size-sorted (*i.e.*, coarse fragments on the bottom of unit and finer fragments at top of unit; Shoemaker, 1974). Mixed debris was probably deposited beyond the crater rim on top of the ejecta blanket, although it has since been stripped away by erosion, except in a small number of locations (Chapter 18; Kring *et al.*, 2012). Fragments of the type of material found in the mixed debris unit are found in younger (post-impact) alluvium terraces that surround the crater.

Post-impact erosion and sedimentation has modified the crater interior, which is evident in both the aerial image of the crater (Fig. 4.1) and the geologic map (Fig. 4.4). Talus and finer debris components have collected at the base of the crater walls, reducing the steepness of the crater walls. Although the topography of the crater is still dramatic, erosional reduction of the rim height, shallowing of the crater wall slope, and sediment filling of the crater floor has reduced the observable size of the crater.

A ~30 m (100 ft) section of lake sediments covers the allogenic breccia in the center of the crater. Moving radially outward from crater center, these lake sediments are interfingered with alluvium being shed from the crater walls. After the impact event the climatic conditions became increasingly arid and the lake evaporated, producing a ~1.6 m (10 ft) thick sequence of playa beds (Shoemaker, 1974).

The erosional processes that produced the talus and alluvium deposits continue today, as evident from the large Kaibab boulders strewn about the crater floor and continuous loss of the fragile allogenic and mixed breccia deposits that cling to the crater walls. Multiple cubic yards of these scientifically valuable breccias are sometimes lost each year.

To help readers correlate the surface geologic units described above with the observable landscape, I have produced an overlay (Fig. 4.6) of Shoemaker's geologic map and an aerial photograph.

Our ability to extend this surface geology downward into the subsurface is greatly enhanced by extensive drilling and deep shafts that were excavated during mining operations at the crater, augmented by later subsurface imaging using several geophysical techniques.

Between 1903 and 1908, the Standard Iron Company drilled 28 holes in the crater floor (maximum depth 1,085 ft or 323 m), excavated 7 shafts on the crater floor (maximum depth of 222 ft or 68 m), excavated 6 shafts on the southern ejecta blanket, excavated 1 shaft on the northern ejecta blanket, excavated 1 shaft just beyond the northern ejecta blanket, and excavated several trenches in the ejecta blanket at sites distributed around the entire crater (Barringer, 1910). Fairchild (1907) reports there were more than 50 pits and trenches on the external slopes of the crater.

Many of the boreholes were reamed with a toothed, hardened steel bit that produced a 2½ inch core, if the rock had sufficient structural integrity (Fairchild, 1907). Because of its inherent weakness, most material in the breccia lens was washed upward by flowing water in the form of disaggregated chips and sand. Only large boulders in the breccia lens and bedrock below the breccia lens were recovered in core form (*e.g.*, in holes 4, 6, 7, and 8). Unfortunately, none of that core material survives.

The boreholes drilled in the crater floor indicate the breccia lens bottoms at a depth of 600 to 700 ft (180 to 210 m) (Table 4.1), which corresponds to the base of the Coconino (Shoemaker, 1960; Roddy, 1978). These boreholes provided the data used to estimate the depth of the breccia lens in Shoemaker's

cross-section of the crater (Fig. 4.5). According to Shoemaker (1974), the Supai Formation was recovered at depths exceeding 700 ft (210 m), whereas Fairchild (1907) reports red beds of the Supai were encountered at depths of 830, 860, and 870 ft (253, 262, and 265 m) beneath the crater floor. Seismic refraction data (Ackermann *et al.*, 1975) is consistent with a breccia lens that bottoms ~190 m beneath the crater floor. The seismic refraction data also suggest the target rocks are fractured beneath the ejecta blanket to distances of 900 m beyond the crater rim and to a depth of at least 800 m below the crater floor and possibly to the crystalline basement.

Holsinger wrote in a letter (as reported by Fairchild, 1907) that a large slab of Coconino slumped down the crater wall during the formation of the breccia lens. Several boreholes northeast of the main shaft encountered a block of the sandstone at depths ranging from 160 to 200 ft before punching through it. The slab is 250 to 400 ft (76 to 122 m) thick, dips at an angle of 40°, and covers 4 to 5 acres (1.6 to 2.0 x 10⁴ m²). Approximately 100 ft of breccia is above the slab and more than 100 ft is below it. Meteoritic material occurs in the breccia beneath the slab.

The United States Refining, Smelting, and Mining Company drilled the deepest exploration hole at the crater on the south rim in 1920-1922 and drove a nearly 400-ft long adit or drift into the wall of the crater when the drill stem broke and drill tools were lost at a depth of 311 ft. After the drilling tools were recovered at the end of the adit, drilling continued until a final depth of 1,376 ft (419 m) was reached, which is approximately 827 ft (252 m) (per Hager, 1953) beneath the level of the crater floor. Not only did the adit solve the drilling problem, it also penetrated meteorite-bearing mixed debris between the talus and crater wall, suggesting additional mixed breccia may survive beneath a protective sheath of talus if needed for future research.

Interestingly, the deep borehole encountered several hundred feet of breccia with Ni traces and an apparent concentration of meteoritic debris in the final 30 feet of the hole (Barringer, 1924; see also Table 4.2, which is a log of this borehole). If the borehole was plumbed vertically, then this breccia lies far outside the transient crater. Thus, there is a discrepancy between the symmetrical view of the breccia lens represented by Fig. 4.5 and the borehole data of Barringer. Shoemaker was aware of the drill hole data and the discrepancy it represented, but was unable to resolve the conundrum.

Some possible solutions: (a) breccias and the transient cavity extend beneath the south rim, which, as interpreted by Barringer, might imply something about the trajectory of the impacting asteroid; (b) the drill hole may have curved towards the crater center while descending and essentially intersected a crater cavity with a geometry similar to that inferred by Shoemaker in Fig. 4.5; or (c) a vein, network of veins, or some other horizon of meteoritic debris and/or breccia was injected into the wall of the transient crater cavity and into the surrounding Coconino bedrock. The first solution defies our current understanding of transient crater cavities, unless strong asymmetry was caused by an oblique impact. The second solution is uncomfortable, because the adit that intersects the drill hole at a depth of 311 feet suggests the hole is vertical. The hole would have had to curve tremendously at greater depths to pierce the breccia lens depicted in Shoemaker's cross-section. The third option is also uncomfortable, because the breccia beneath the rim is several hundred feet thick, which, if taken at face value, implies an injection of material far larger than that considered feasible in the past. I suspect (c) is the correct solution.

Seismic refraction (Ackermann *et al.*, 1975) and gravity (Regan and Hinze, 1975) data paint an independent image of the breccia zone. A model derived from the seismic refraction data suggests the breccia lens is symmetrical, concentrated in the center of the crater, and does not, at depth, extend to the diameter of the crater (Fig. 4.7). A model of the gravity at the crater also suggests the breccia lens is concentrated in the center of the crater and does not, at depth, extend to points beneath the crater rim (Fig. 4.7). An asymmetric feature is recognized on the south side of the crater, but it suggests the breccia

lens is less wide (not wider) towards the south. Thus, these geophysical models are generally consistent with Shoemaker's cross-section through the breccia lens.

The seismic refraction data, however, also suggests a possible explanation for the breccia and meteoritic components in the 1,376 ft borehole. It is clear that the walls of the transient crater (that is, the bedrock beyond the breccia lens) was highly fractured by the impact event. The seismic model includes fractured bedrock to within ~150 m of the bottom of the 1,376 ft borehole. It is possible that the breccia encountered in the borehole represented fractured wall rock, rather than the breccia lens. It is also possible that the traces of meteoritic material represent veins of material injected into that crater wall, producing the Ni-traces seen several times while the drill passed through the fractured wall rock. This requires, however, the injection of meteoritic material nearly 300 m beyond the walls of the transient crater with a radius of ~500 m and depth of ~300 m. The magnitude of brecciation may have been greater than that depicted in Fig. 4.7, if either the zone of fracturing was wider than in the model or if the drill curved towards the crater center. Thus, one might be able to explain the occurrence of breccia and meteoritic material in the hole and still be consistent with estimated dimensions of the breccia lens. The remaining problem is the rather thick (Barringer estimated 30 ft thick) zone of oxidized asteroid at the bottom of the hole. This would seem to require an unusually large vein of injected material in the crater wall. A completely satisfying explanation will probably escape us, unless a series of new boreholes, with coring capabilities, are drilled on the crater floor and crater rim. I hypothesize shatter cones exist along the path from the crater wall to the bottom of the 1,376 ft borehole. Interestingly, traces of impactor material have been found on the surfaces of shatter cones in other impact craters (*e.g.*, Schmieder *et al.*, 2015).

Additional drilling occurred after the 1,376 ft hole was completed, but it did not resolve the origin of the Ni traces beyond the transient crater wall. In 1928, the Meteor Crater Exploration and Mining Company began the final phase of mining operations with three more drill holes (maximum depth 721 feet) in the same area as the 1,376 ft hole. The company then sank a final shaft at the crater from June 1928 through mid-July 1929, when the shaft reached a final depth of 713 ft. Operations stopped there because of flooding. Further exploration of the meteoritic debris beneath the south rim was never pursued further.

Drilling operations were renewed several decades later, but in this case for scientific purposes in support of the Apollo program. The USGS, under contract to NASA, drilled 5 holes on the south rim in 1965-1966 (maximum depth of 366 ft) and excavated a single trench to provide physical information for lunar analogue studies. The USGS also drilled 116 holes through the ejecta blanket and 45 holes beyond the ejecta blanket in the early 1970's. Some of this latter material survives and is available for credible research projects from the USGS.

Roddy (1978) collated the above drilling and geophysical data and converted the structural depths to values relative to the pre-impact surface. He determined that the average pre-impact surface elevation was $1,683 \pm 2$ m. He estimated the distances from that surface to the top of the fallout, top of breccia lens, base of breccia lens, and base of fractured rock are ~150, ~160, ~310, and 990 m, respectively. He also estimated the average height of the structural uplift in the rim is ~47 m above the pre-impact surface and that the pre-erosion thickness of ejecta on the rim was $\sim 20 \pm 5$ m, with the caveat that the latter was variable.

Beginning with Shoemaker's (1960) comparison of Meteor Crater with nuclear explosion craters (see also Short, 1964) a picture of the processes involved in the crater's formation has matured. Details about the trajectory, energy, and several other parameters are still being debated in the community, but several general attributes of the processes that created the crater can be summarized with two generic

graphics (Fig. 4.8 and 4.9). The impacting asteroid penetrated the Moenkopi surface to a depth approximately equal to its diameter and, in an explosive release of its kinetic energy, generated a downward and laterally radiating shock wave. As that shock wave radiated through an increasingly larger volume of rock in the Earth's crust, peak shock pressures declined. Thus, the highest, vapor- and melt-producing shock pressures occurred near the point of impact.

A shock wave simultaneously radiated upward through the projectile, producing a reflected rarefaction wave that then radiated downward into the target. After the shock wave and rarefaction wave passed through a section of the Earth's crust, a residual particle velocity was imparted on the material. The effect of that velocity was to establish a flow of rock that initially moved downward and radially outward, before moving upward and outward. This is the flow of material that excavated the crater cavity and ejected debris onto the surrounding landscape. Material remaining along the crater walls slumped inward, forming a breccia lens. Depending on the energy of an event, that breccia lens may incorporate impact melt fragments. In the case of Barringer Crater, which is one of the smallest hypervelocity impact craters, very little melt appears to have been incorporated into that breccia lens. The total time involved in this dramatic re-organization of rock, melt, and vapor was only a few seconds.

Morphological and geophysical data were recently used to constrain numerical models of the impact processes that produced the final structure of the crater and its associated gravity anomaly (Collins *et al.*, 2016). Impact speeds, impactor physical states (*e.g.*, one coherent dense mass or a ruptured lower-density cloud of iron fragments), and target properties were investigated. The best fit to the final crater diameter, rim height, and depth to the top and bottom of the breccia lens was generated by an impact speed of 15 km/s, impactor mass of 3.2×10^8 kg, and damaged target cohesion of 50 kPa. For a discussion of the important role of dilatency and other details of the impact process, I refer readers to Collins *et al.* (2016) and the subsequent final report (in preparation). For our purposes here, Gareth Collins (personal communication, 2017) kindly replotted output parameters to illustrate the distribution of shock pressures as mapped onto pre-impact target locations and in the final crater (Fig. 4.10).

A discussion of the details involved in this generalized impact cratering scenario, like the trajectory and energy of impact, are discussed in later chapters.



Fig. 4.1. Overhead aerial view of Barringer Meteorite Crater. The crater is ~1.2 km in diameter. The central depression is ~180 m deep and the crater rim rises 30 to 60 m above the surrounding plain. North is at the top of the image and the sun is illuminating the crater from the SSE, creating shadows beneath the cliffs in the southern crater wall and, to a lesser extent, beneath the cliffs in the eastern crater wall. The current museum complex is located on the NNE crater rim. Remnants of mining operations are visible on the crater floor, the south crater wall, and on the SW flank of the crater. Two-needle pinyon pine and juniper dot the southern flank of the crater and the uppermost southern crater wall. Several faults cut through the crater wall and rim sequence. The crater is a modified circle, with slightly squared corners that are associated with those tear faults. The faults may have been activated along pre-existing joints in this portion of the Colorado Plateau (*e.g.*, Shoemaker, 1960).

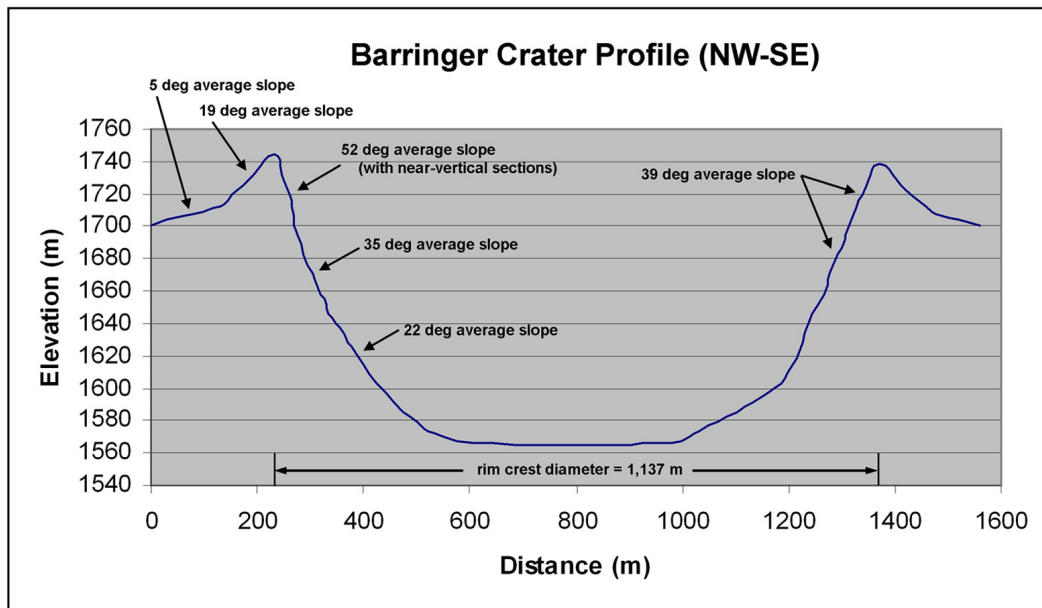
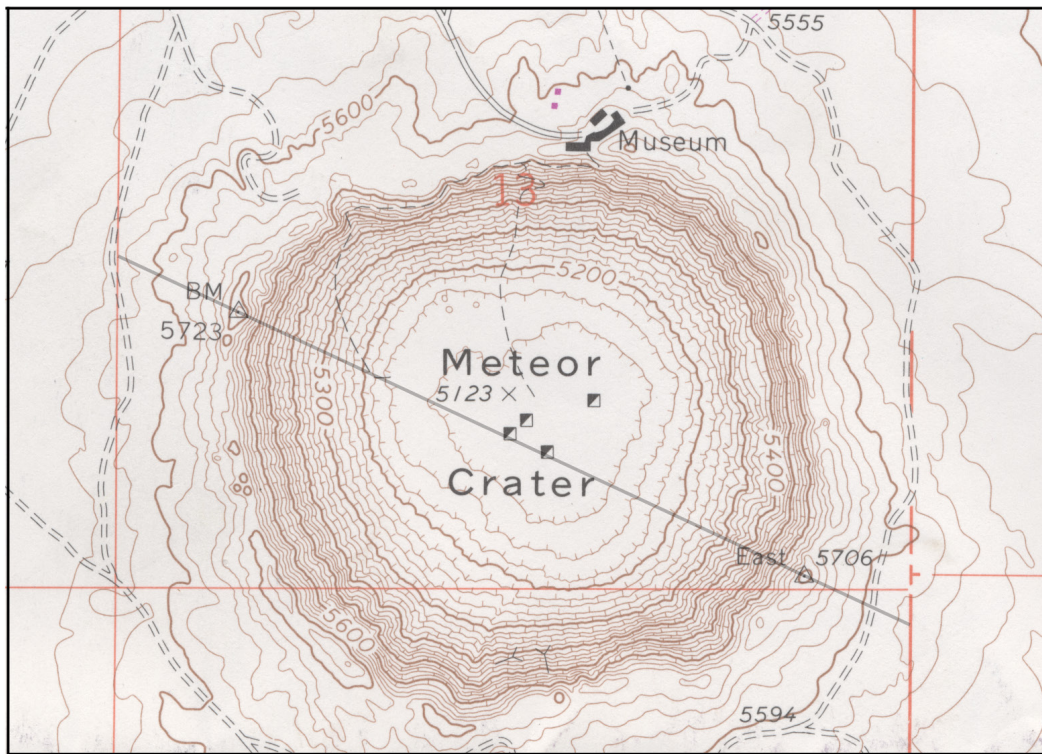


Fig. 4.2. Topographic map of the crater (top panel) as presented on the current USGS 7.5 minute quadrangle for Meteor Crater. The map is contoured in 20 ft intervals. Barringer Point (5,723 ft) is one of the highest locations on the crater rim. A line drawn across the map from NW to SE indicates the location of a cross-section through the crater (bottom panel). The cross-section is calibrated in meters and is vertically exaggerated. Slopes in the upper crater wall average ~50 degrees and include near vertical cliffs.

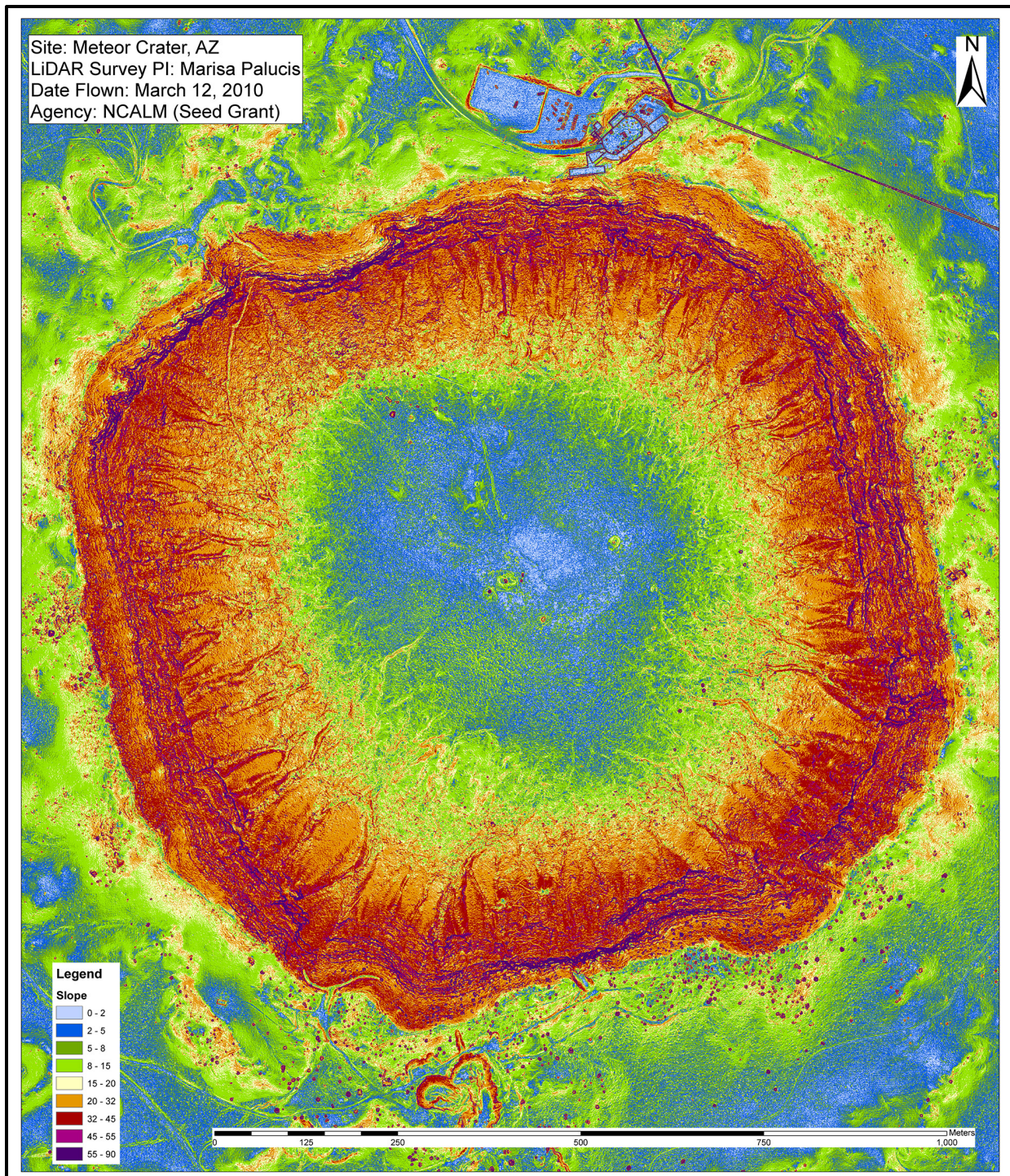


Fig. 4.3. New LiDAR techniques are enhancing the resolution available for studies of the crater. Here, for example, is a slope map that Palucis produced from a new aerial LiDAR survey conducted in 2010. This slope map and the source digital elevation map (DEM) with 25 cm resolution highlight many features not easily discerned any other way. The data were initially applied to a study of gullies on the crater wall (Palucis *et al.*, 2012a,b). These and other electronic data are curated at the Lunar and Planetary Institute (LPI) along with an electronic copy of this guidebook. The url is http://www.lpi.usra.edu/publications/books/barringer_crater_guidebook/.

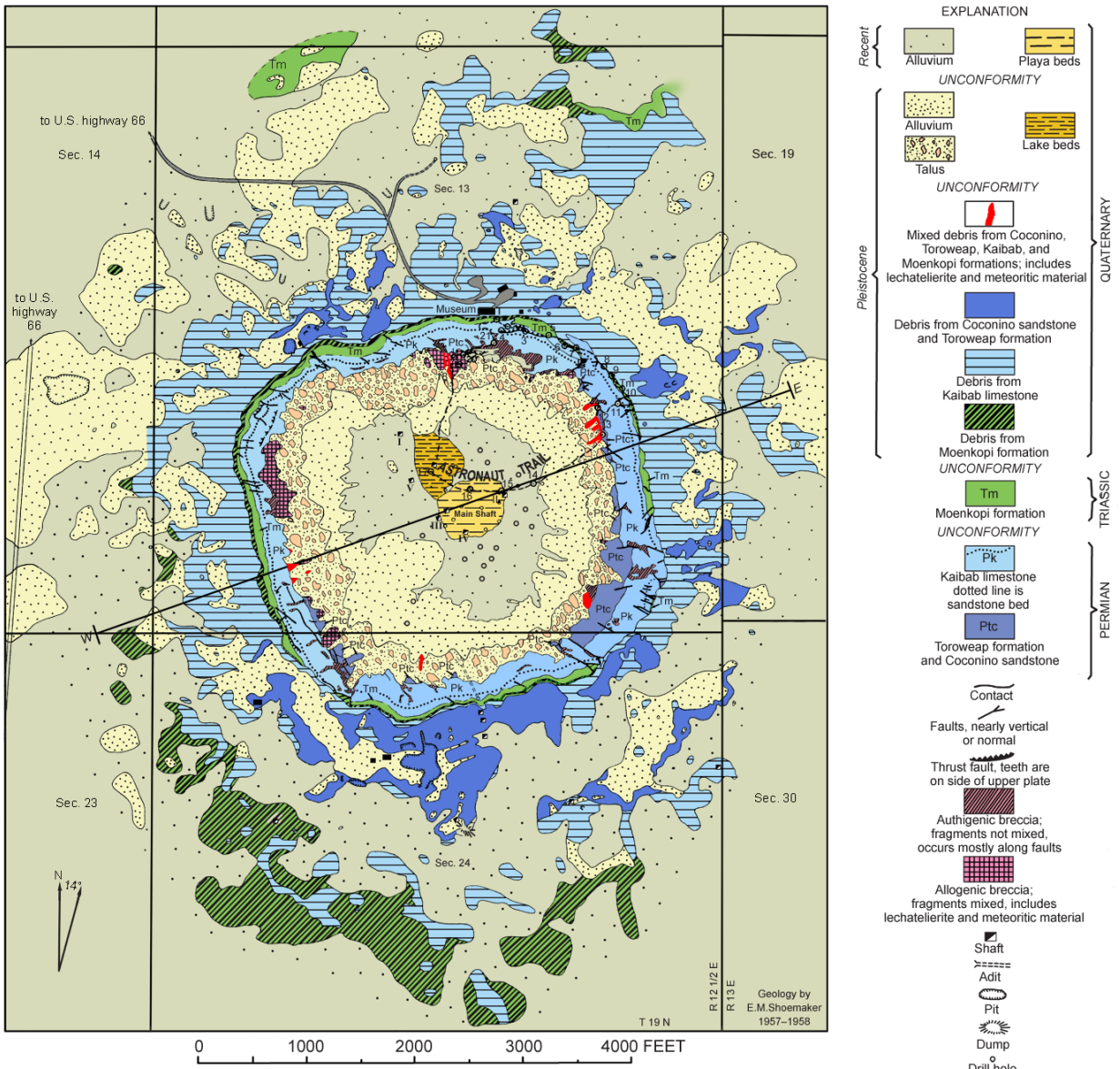


Fig. 4.4. Geologic map of Meteor Crater, Arizona, produced by Eugene M. Shoemaker (1960). In addition to locating the bedrock lithologies (Coconino-Toroweap, Kaibab, and Moenkopi), he also mapped the interior breccia deposits, exterior debris deposits, and faults that cross-cut the crater walls. Many of the features represented by this map had previously been identified by Barringer (*e.g.*, 1905), but Shoemaker mapped them in exquisite detail and provided useful comparisons to geologic features produced in a nuclear explosion crater. This figure is a colored version of Shoemaker's original map. Target lithologies visible in the crater walls are the Permian Toroweap and Coconino sandstones (undivided, Ptc), Permian Kaibab Formation (Pk), and Triassic Moenkopi Formation (Tm). Over-turned and ejected Quaternary debris from those units are identified with diagonal hatching (Moenkopi ejecta), horizontal hatching (Kaibab ejecta), and a different shade of color (Coconino ejecta). Impact-generated breccias are identified with different shades of red and pink. A west-east cross-section across the structure is shown in Fig. 4.5. Color added by Kring (2007).

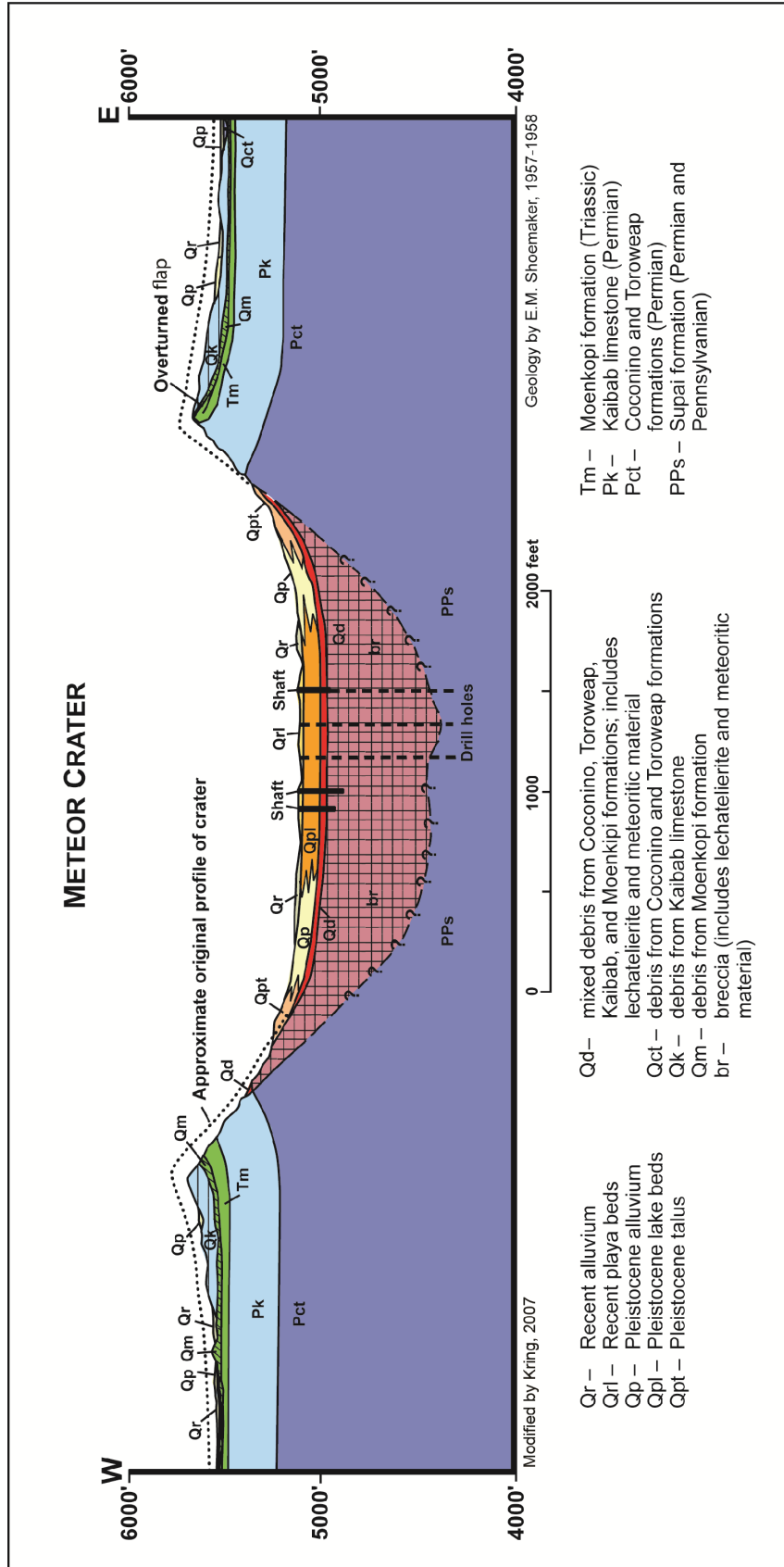


Fig. 4.5. Structural and lithological cross-section through Meteor Crater along a W-E axis. See Fig. 4.4 for the location of the W-E axis and Shoemaker (1960) for the original presentation of this cross-section. The breccia (Br) refers to the allogenic breccia described in the text. The mixed debris unit (Qd) refers to the mixed debris unit or fall-back breccia described in the text. Although not precisely defined in drill core and, thus not marked in the cross-section, the boundary between the Coconino Formation (Pct) and underlying Supai Formation (PPs) is near the bottom of the breccia lens. The cross-section has been redrawn from Shoemaker (1974) and keyed in color.

Table 4.1. Partial summary of exploration boreholes and shafts produced by Standard Iron Company on the crater floor

Hole No. or Shaft No.	Radial distance from Main Shaft (ft)	Approx. bearing of hole or shaft from crater center (ft)	Approx. elevation at top of hole (ft)	Total depth of hole (ft)	Depth of hole normalized to 5135 ft datum (ft)	Thickness of lake sediments (ft)	Depth to Variety A sandstone (ft)	Range of Ni-bearing material (ft)	Depth to solid rock (ft)
Main Shaft	0	-	5135	222	222	-	-	-	-
2	80	230	-	-	-	-	-	-	-
8	90	125	5135	1085	1085	-	-	-	1030
Shaft III	100	230	5135	-	-	-	-	-	-
1	110	235	-	-	-	-	-	-	-
4	120	180	-	-	-	-	-	-	-
3	130	185	-	-	-	-	-	-	-
23	160	65	-	800	-	-	40	520-620	660
6	200	0	5135	1059	1059	-	-	-	1030
5	250	230	5140	1003	998	-	-	-	-
Shaft IV	250	135	5135	>15	-	-	-	-	-
22	300	45	-	860	-	-	30	600-620	650
7	320	135	5135	960	960	-	-	450-550	-
Shaft VI	320	345	5140	36	31	35	-	-	-
20	330	75	5135	780	780	-	40	640-680	720
12	380	110	5135	881	881	60	60	595-640	700
11	440	165	5135	830	830	-	-	-	640
14	460	125	5135	780	780	-	50	540-620	670
13	480	100	5135	740	740	-	20	598-660	640
21	500	75	-	760	-	-	20	620-640	660
Shaft II	510	70	5135	145	145	100	-	-	-
16	570	110	-	750	-	-	20	540-620	640
9	590	140	5140	670	665	-	-	-	-
Shaft V	600	310	5140	>15	-	-	-	-	-
15	620	125	5140	750	745	-	50	590-600	650
10	650	155	5150	745	730	-	-	-	640
17	650	100	5140	720	715	61	40	520-580	600
19	730	85	5140	680	675	-	-	-	620
Shaft I	740	330	5155	>15	-	-	-	-	-
18	800	100	5150	660	645	-	-	-	630
24	-	-	5140	-	-	-	-	550-650	-
1**	1750	-	5684	1376	827	-	-	? - 1376	-

Sources: Merrill (1908) and Hager (1953) for borehole data; elevations at top of holes determined by correlating numbered hole positions on Barringer's (1910) map with un-numbered hole positions on a current USGS 7.5 min quadrangle topographic map

* Merrill provides a range from 450 to 584 ft, whereas Hager provides range of 550 to 584 ft; Merrill's value of 450 ft is consistent with Barringer (1910)

** Hole drilled by U. S. Smelting, Refining, and Mining Company on south crater rim

Table 4.2. Log of 1,376 foot deep churn drill hole on south rim of Meteor Crater*

Drilling by U. S. Smelting, Refining, and Mining Company
 L. F. I. Holland, drilling superintendent to 326 ft; C. W. Plumb, drilling superintendent to 1,376 ft
 Drilling began November 1920; drilling completed November 1922

Depth from (ft)	to (ft)	Description
0	174	Limestone. Many crevices in limestone
174	195	{Interval not logged}
195	200	Sandstone. Lighted center goes out of sight. White, loose
200	250	Limestone. Drilling past broken cores
250	257	Limestone. Particles of shale ball
257	283	Limestone
282	288	Limestone. Sand commenced to show in bailings
288	290	Brown and yellow stained saccharoidal sand. Much iron and steel, no nickel
290	311	Sand
311	312	Lost hole. Underreamer at bottom
312	326	In tunnel 71-vesicular sandstone
326	380	White sandstone, very quick. 375' hard material dropped in hole
380	384	Drill twisted off
390	425	White sandstone
425	460	White sandstone
460	464	Red cong. Or coarse red sandstone. Small shells, 1/8" long
464	468	Red clay-streaks of white calcite
468	480	Red or cong. or coarse red sandstone
480	500	Red sandstone or conglomerate. Steel
500	520	White sandstone
600	603	White sandstone
603	605	Hard conglomerate
605	607	Hard conglomerate
607	615	Possibly white sandstone with reddish streaks
615	620	Hard conglomerate
620	627	Whitish sandstone
627	669	White sandstone
669	684	White sandstone (?), red sandstone at bottom
684	725	Red sandstone. Hard to get samples
725	750	Crevice. Coarse grains of limestone, sandstone, and silica
750	801	Red mud or clay, white streaks
801	820	Red clay with calcite streaks
820	876	Large crevice. Rounded pebbles of limestone, silica, and sandstone. Iron nodules, all cemented
876	930	Same conglomeratic material
930	940	Conglomerate as above
940	942	Red clay
942	953	Red clay
953	957	Iron nodule. No nickel
957	1096	Alternating layers of white and gray sandstone. Drilled easily
1096	1100	Hard drilling, iron nodule, no nickel
1100	1130	Hard nodules, similar to 958. Segregations from sandstone, filled with small black particles-silicon, effervesces readily
1130	1287	Hard boulders in siliceous white sandstone. 1" to 6". Some nodules show nickel reaction-perhaps shale balls. Some greenish material, looks like clay
1130	1134	4' very hard, like rest of boulders
1134	1145	Soft sandstone. Small greenish pieces of metal or slag in sample. Slight show of nickel
1145	1168	Hard and soft material, slight nickel, layers 6 inches to one-foot layers
1168	1187	Very soft, white silica sand. Then hard and white like silica sand found in crater
1187	1188	Five hours, sample very black, heavy, greenish pieces of metal, very strong nickel
1188	1190	Same as above
1190	1208	First foot hard. Then alternate hard and soft in 6 inches to one foot
1208	1228	Very soft for 15', then hard and rough. Good test of nickel. Silica sand almost transparent
1228	1251	2' hard, rough. Five hours on last foot, stray nickel
1231	1235	4' hard, rough
1235	1249	Silica sand, medium soft. Slight nickel
1249	1271	Soft, white sandstone. Hard nodules at 1,255', 1,260', 1,270'. No nickel
1271	1276	Hard and rough. Like nest of hard boulders. Fine nickel test
1276	1287	Easier for 5 feet. Then harder and rough, fine nickel test
1287	1293	Drilled very hard 4', hard to get samples. Then easier, good nickel
1293	1311	Hard few inches. Then very soft. Fair nickel test
1311	1323	Easy drilling 10', then very rough. Samples quite black. White sandstone and black material about 50 per cent each. Few pieces red sandstone showing. Shells. White sandstone getting harder. Samples show good nickel test
1323	1335	Drilling rough for 7 feet. Then smooth and very hard. Many pieces of <i>hard red sanstone</i> . Also many shells 1/8" long. Fine nickel test
1335	1339	Reamed very hard, like in boulders size of baseball. Drillings looked very black. Samples all gave fine nickel test, about 75 per cent mineral
1339	1350	Drilling hard but smooth. Some red sandstone but mostly black or brownish pieces of material, very magnetic. Best nickel test yet
1350	1352	Hard for 2 feet. Lost sludge at once. Lost circulation. From 1,095' to 1,352' black mineral particles, plentiful
1352	1360	Formation about as last 250 feet. Nickel about same
1360	1370	Formation hard and rough. Shale ball appearance. Last 2500 feet
1370	1376	Extremely hard and rough. Strong nickel test. Samples look as if we are passing through a recemented mass of conglomerate as we find shells, rounded pebbles of red sandstone and of limestone, and also a great many small brown pieces resembling shale balls. Stuck and had to abandon at 1,376 feet. Bit appears to have wedged under boulders

* Hager (1953), who obtained access to drilling record from R. N. Hunt, chief geologist for the U. S. Smelting, Refining, and Mining Company in Salt Lake City, Utah

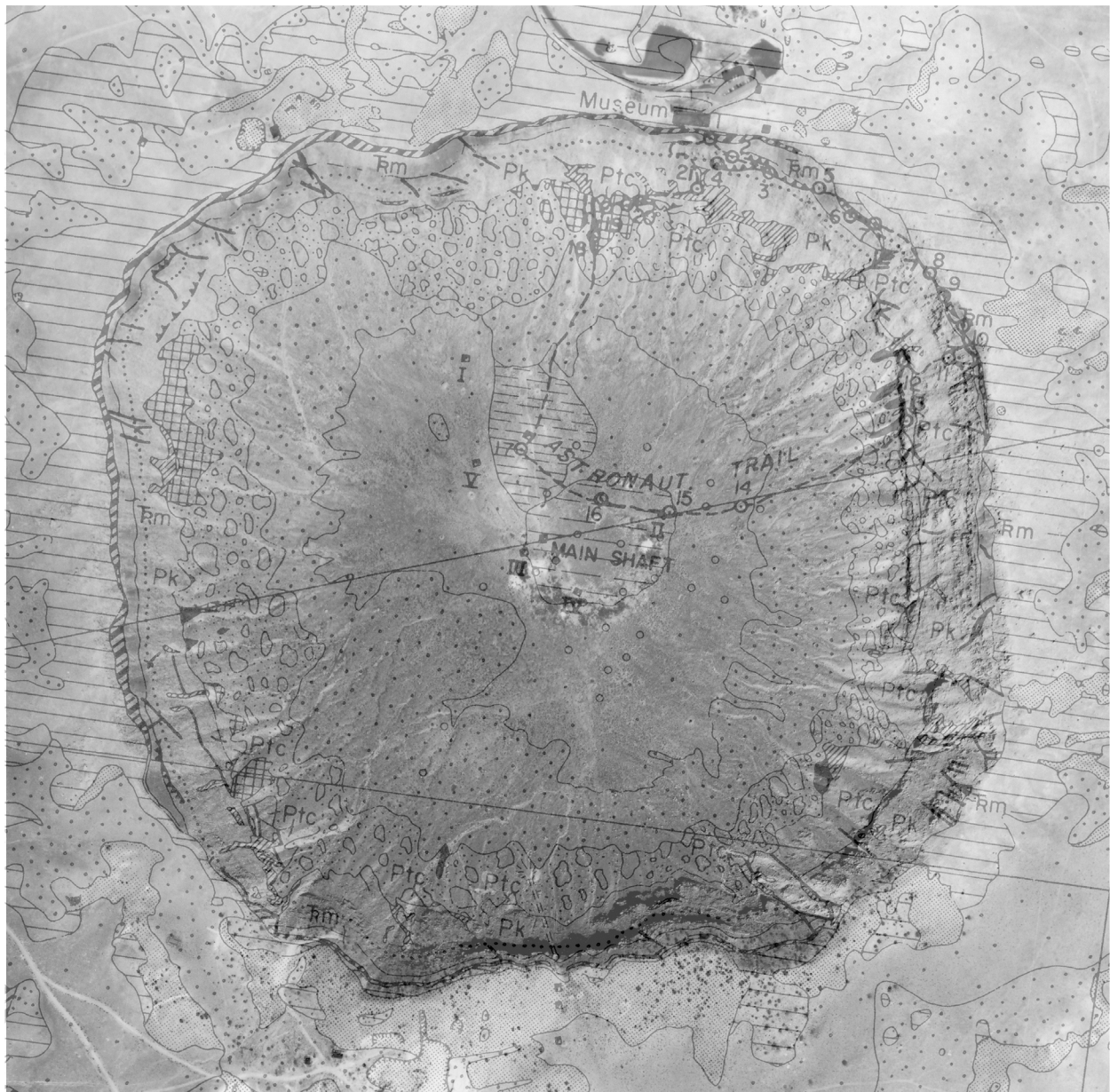


Fig. 4.6. An overlay of Shoemaker's 1960 map with an overhead aerial photograph of the crater. The Astronaut Trail is the route featured during the 1974 Meteoritical Society field trip to the crater, but is severely degraded and no longer functional. The approximate locations of some of the mining features (e.g., main shaft, several smaller shafts, and borehole locations) are marked on the crater floor. See Fig. 4.4 for key to map symbols.

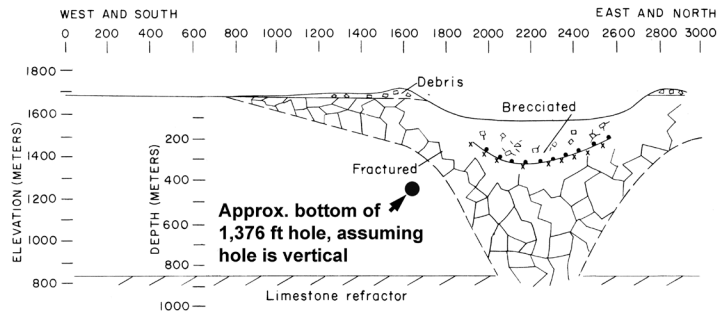
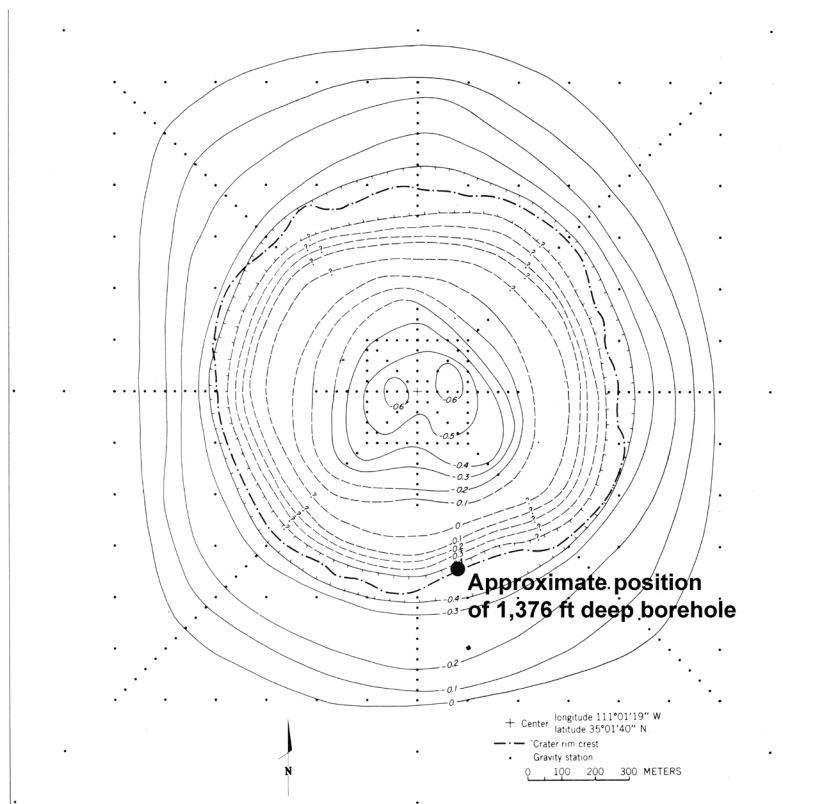
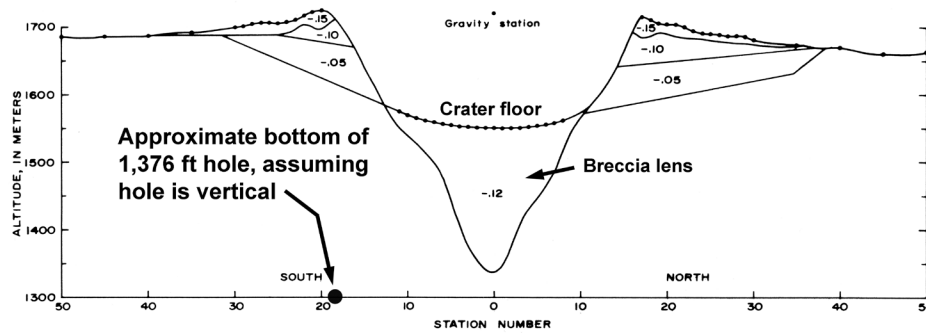


Fig. 4.7. Models of the subsurface structure of Barringer Crater. Model based on seismic refraction data illustrates the extent of ejected debris, the breccia lens, and fractured walls of the crater (top panel). Model based on gravity anomalies illustrates the floor of the breccia lens in a south-north cross-section (middle panel) and in plan view (bottom panel). (Composite illustration based on Ackermann *et al.*, 1975, and Regan & Hinze, 1975.)



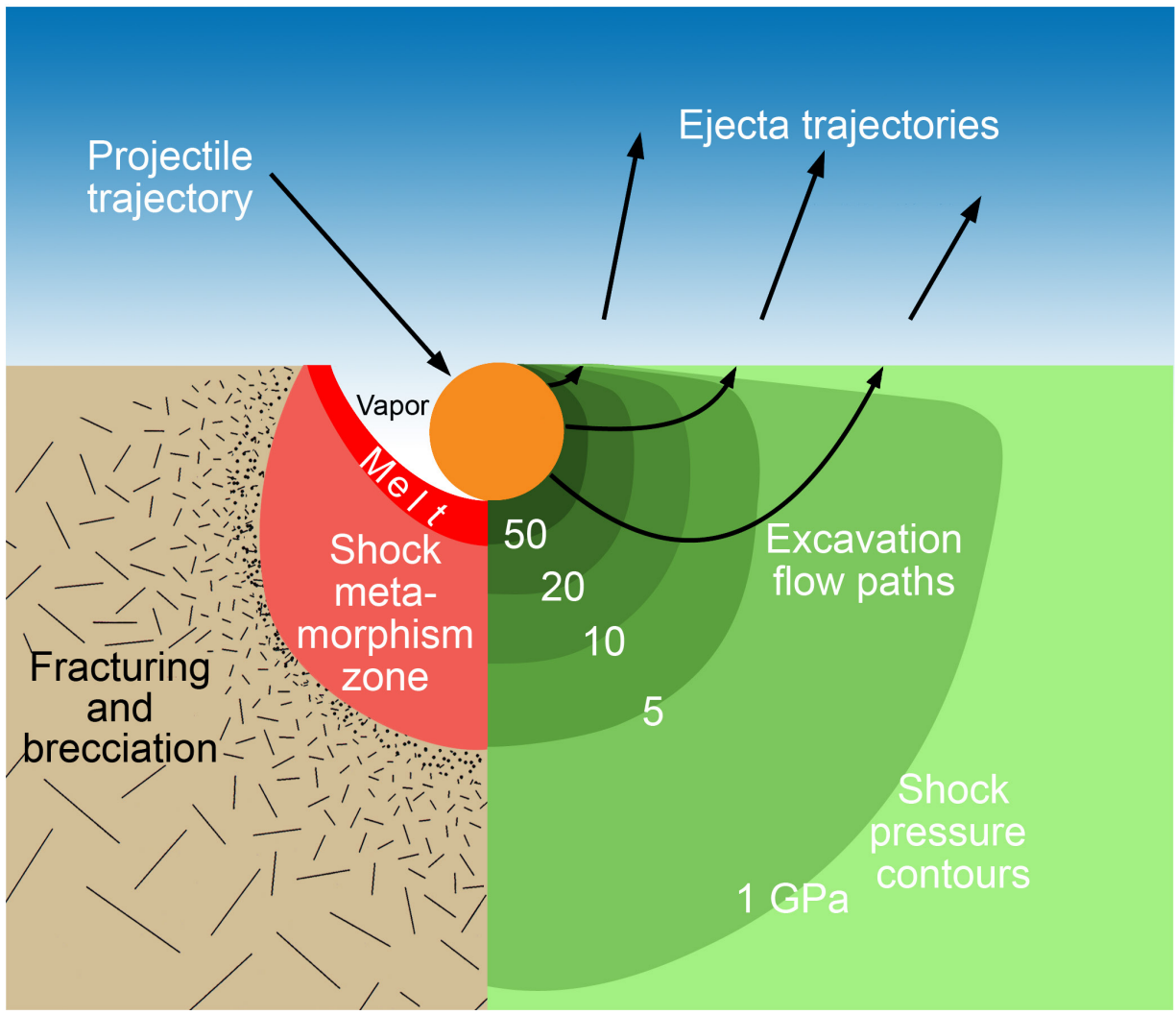


Fig. 4.8. Schematic diagram of the peak shock pressure contours generated during an impact event (right side of diagram) and the type of deformation generated by those shock conditions (left side of diagram). The projectile penetrates to a depth approximately equivalent to its diameter or slightly deeper. The projectile is largely transformed to melt and vapor (the relative proportions of which depend on the energy of the impact event), although a small (<10%) fraction of it may survive as solid fragments. Some of the melted projectile will be mixed with a zone of molten target material (shocked to pressures >50 GPa), but a fraction of it will also be ejected with the vaporized components of the projectile. Shock pressures in the target decrease with distance. Beyond the regions where the target is vaporized and melted, target material will undergo a series of solid state transformations (between shock pressures of ~5 to ~50 GPa), including the production of planar fractures, planar deformation features (or shock lamellae), higher-pressure polymorphs, and diaplectic glasses. At the greatest distances (and lowest shock pressures), the bedrock may be sculpted into shatter cones and fractured. The vaporized, melted, and otherwise shock-metamorphosed material within the transient cavity will flow downward and outward and then upward and outward on paths perpendicular to the shock isobars and ejected into the atmosphere before falling back to the surface on ballistic trajectories. The flow and ejection processes mix material of several different shock levels (including completely unshocked material) and produce complex breccias. (Illustration from an educational poster, Geological Effects of Impact Cratering, David A. Kring, NASA Univ. Arizona Space Imagery Center, 2006. Modified from a figure in *Traces of Catastrophe*, Bevan M. French, 1998.)

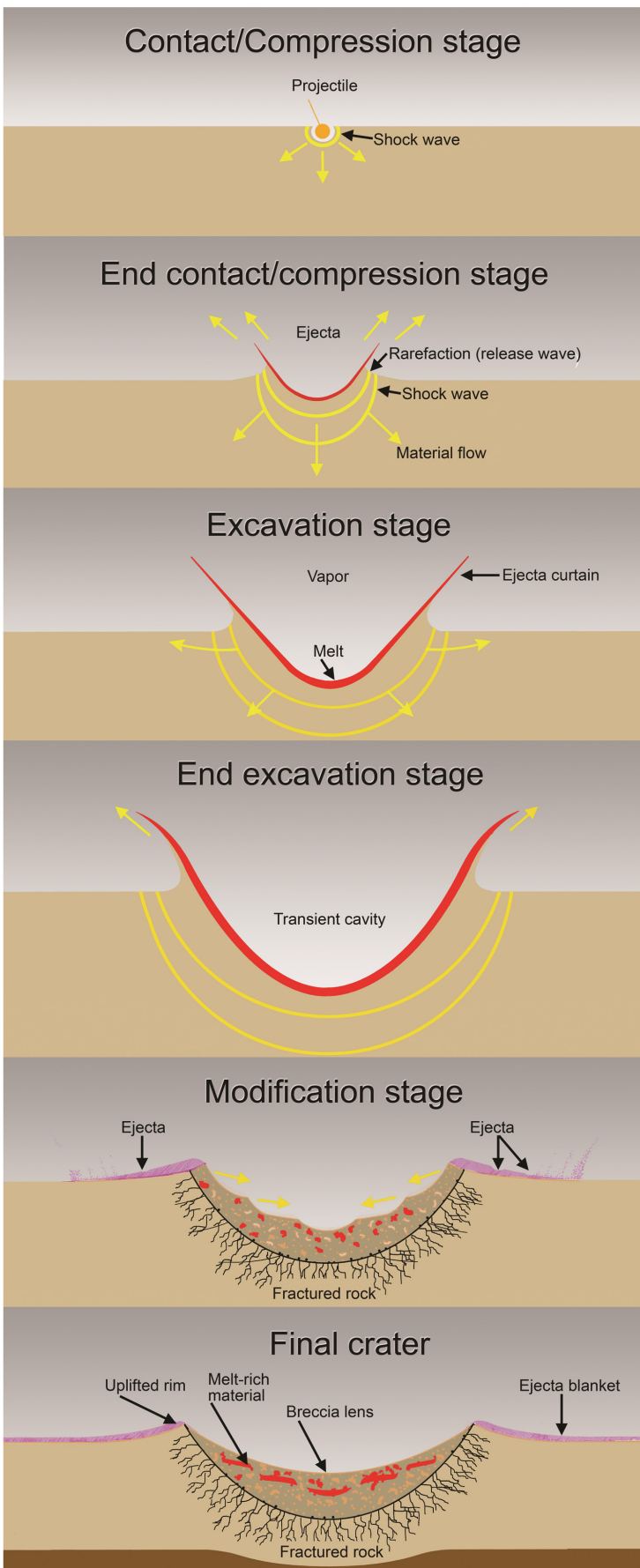


Fig. 4.9. Six views of simple crater formation (generic and schematic). Projectile penetrates the surface and generates a shock wave. A transient crater begins to grow as excavation begins. The transient crater reaches its maximum depth before reaching its maximum radius. When excavation is complete, any remaining debris on the crater walls slump inward to form a breccia lens. Melt will be distributed in the ejecta and any material that falls back on top of the breccia lens. If the crater-forming event is energetic enough, then melt will also be incorporated into the breccia lens. (Illustration from an educational poster, Geological Effects of Impact Cratering, David A. Kring, NASA Univ. Arizona Space Imagery Center, 2006. Modified from a figure in *Traces of Catastrophe*, Bevan M. French, 1998.)

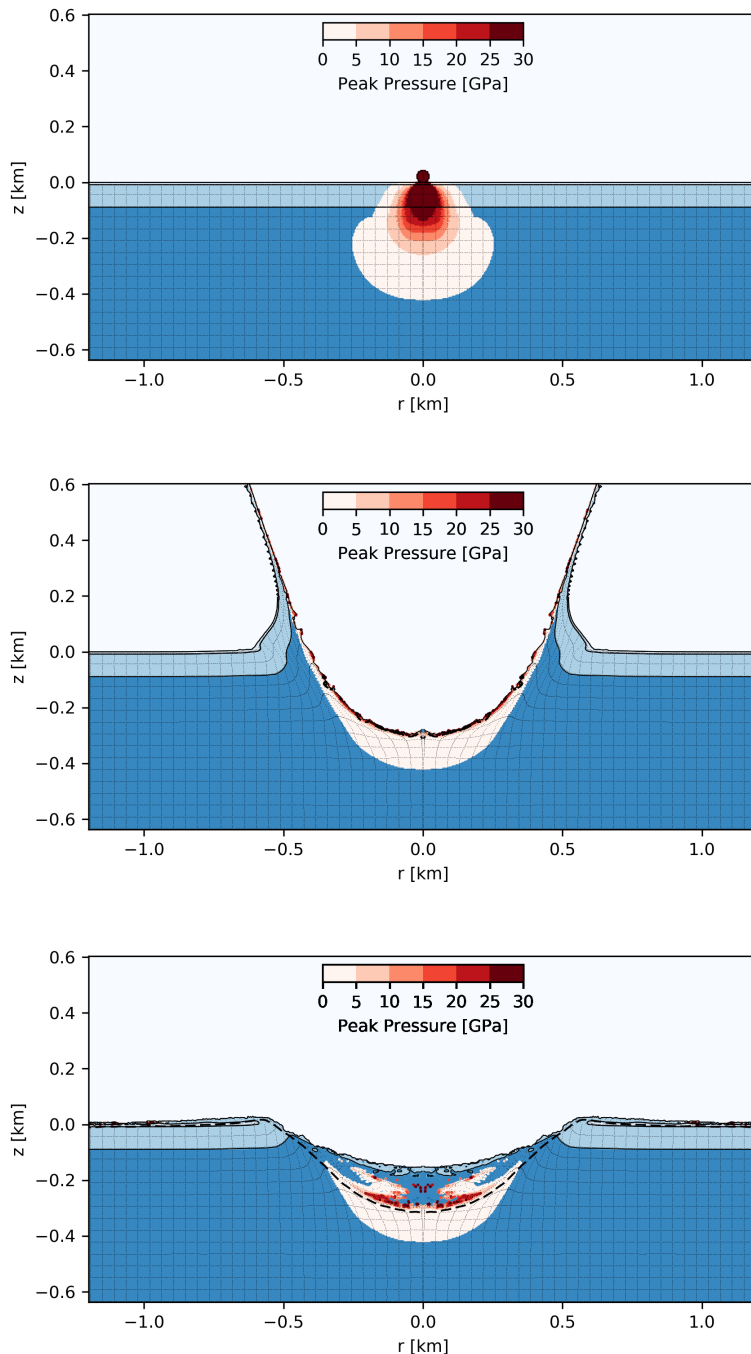


Fig. 4.10 As described in a preliminary report (Collins *et al.*, 2016), computer models of the impact have been made to better understand the formation of simple craters in layered sedimentary targets. The target was modeled with 8.5 m porous (18%) dry sandstone (Moenkopi); 80 m porous (19%) dry limestone (Kaibab); 37.5 m porous (22%) dry sandstone (Toroweap and upper Coconino); and wet sandstone (deeper, water-saturated Coconino). Shock pressures are color coded from 1 GPa to 30 GPa. Melting of these lithologies may begin at ~30 GPa (Wünnemann *et al.*, 2008), but potentially as low as 20 GPa (Kowitz *et al.*, 2016). The top panel illustrates shock pressure distribution within that target. The middle panel shows the transient crater forming. The bottom panel illustrates the final crater with a dashed line along a strain contrast representing the base of the breccia lens. The distribution of shock pressures seen in material along the base of the breccia lens is accurate, because tracer density in the models is good in that location. The tracer density is poor in the middle to the top of the breccia lens, so the absence of highly shocked material there may not be real. These panels are kindly provided by Gareth Collins for this guidebook ahead of his own publication of the final model results.

